CrossMark

A Real-time View of Orbital Evolution in HM Cancri

Tod E. Strohmayer
Astrophysics Science Division and Joint Space-Science Institute, NASA's Goddard Space Flight Center, Greenbelt, MD 20771, USA
Received 2021 February 12; revised 2021 March 26; accepted 2021 March 31; published 2021 April 29

Abstract

HM Cancri is a double degenerate binary with the shortest orbital period presently known. The 5.36 minute period is seen as a large amplitude, soft X-ray modulation, likely resulting from a hot spot produced by direct impact accretion. With such a short orbital period it is expected to have a gravitational wave luminosity comparable to or larger than that in the X-ray, and its orbital frequency is known to be increasing at a rate consistent with the expected loss of angular momentum due to gravitational radiation. We use recent Neutron Star Interior Composition Explorer observations to extend its long-term X-ray timing baseline to almost 20 yr. Phase coherent timing of these new data combined with existing Chandra data demonstrates conclusively that the rate of orbital frequency increase is slowing, and we measure a nonzero $\ddot{f}_0 = -8.95 \pm 1.4 \times 10^{-27}$ Hz s^{-2}, which is to our knowledge the first such measurement of its kind for any compact astrophysical binary. With the simultaneous high precision measurement of $\dot{f}_0 = 3.557 \pm 0.005 \times 10^{-16}$ Hz s^{-1}, we estimate that the system will reach its maximum orbital frequency of $f_{max} \approx 3.1172091$ mHz in 1260 ± 200 yr, indicating that the system is close to its epoch of maximum orbital frequency. Assuming mass transfer is conservative, the measurement of $\ddot{f} < 0$ implies that the accretion rate from the donor is growing, with $-5.4 \times 10^{-10} < \ddot{M}_2 < -4.0 \times 10^{-10}$ $M_\odot$ yr^{-2}. Further quantitative comparisons with theoretical models should enable more precise inferences regarding its current evolutionary state.

Unified Astronomy Thesaurus concepts: White dwarf stars (1799); Compact binary stars (283); Interacting binary stars (801); X-ray binary stars (1811); Accretion (14); Orbital evolution (1178); X-ray sources (1822); AM Canum Venaticorum stars (31)

1. Introduction

Double degenerate systems containing a pair of white dwarfs are the most compact binary systems known and can theoretically have orbital periods shorter than 5 minutes (Tutukov & Yungelson 1996; Nelemans et al. 2001). Their evolution is largely driven by the loss of angular momentum due to emission of gravitational radiation, and they are highly anticipated targets for space-based gravitational wave detection with LISA (Amaro-Seoane et al. 2017). They are likely the progenitors of at least some type Ia SN and may also represent a substantial fraction of supersoft X-ray sources (Hils & Bender 2000; Nelemans et al. 2004).

Two such systems (one confirmed and one strong candidate) are of particular interest as pulsating, soft X-ray targets for unique, quantitative studies of their orbital evolution. Both HM Cancri (HM Cnc, also known as RX J0806.3+1527) and V407 Vul (a.k. a. RX J1914.4+2456) show ≈100% soft X-ray modulations at their putative orbital periods of 5.4 and 9.5 minutes, respectively (Israel et al. 2003; Strohmayer 2004, 2005). Radial velocity modulations in optical emission lines at the 5.4 minute period of HM Cnc were measured by Roelofs et al. (2010), definitively confirming its ultracompact binary nature, in fact, it is the most compact binary system presently known. While similar measurements have not yet been made for V407 Vul, the systems are so similar in both their X-ray and optical modulation properties that it too is almost certainly an ultracompact binary. For the remainder of this paper we focus on HM Cnc.

The component white dwarfs in HM Cnc are only separated by ≈0.1 $R_\odot$, so close that the accretion stream plows directly into the accretor without forming an accretion disk, so-called direct impact accretion (Marsh & Steeghs 2002; Roelofs et al. 2010). The impact stream creates a hot spot on the accretor,

which produces the soft X-ray emission. Orbital motion of the, perhaps, tidally locked components produces the observed X-ray pulse once per binary orbit, as the hot spot is rotated in and out of view by the orbital motion. The optical emission is also modulated at the same period, with the peak of the optical pulse leading the X-ray pulse by about one-fifth of a cycle (Barros et al. 2007). This suggests that the modulated optical emission arises mostly from the hemisphere of the donor that faces the accretor, and that the X-ray hot spot is positioned ≈90°–100° ahead of the line connecting the centers of mass of each component. Here, ahead means in the same direction as the orbital motion. This positioning of the X-ray hot spot is entirely consistent with the expected impact point of the accretion stream in such a binary (Lubow & Shu 1975; Marsh & Steeghs 2002; Barros et al. 2007).

Precision, long-term timing of the X-ray pulses provides a unique probe of binary evolution in the system. Timing measurements to date indicate that the orbital frequency is increasing at a rate $\dot{f} = 3.63 \pm 0.06 \times 10^{-16}$ Hz s^{-1}, the magnitude of which is fully consistent with expectations for loss of angular momentum due to gravitational radiation (Israel et al. 2004; Strohmayer 2005) in such a binary. The orbital evolution in such systems results from an interplay between strong gravitational radiation, which removes orbital angular momentum, thus reducing the orbital separation (increasing the orbital frequency), and the mass accretion rate from the donor, which acts to increase the orbital separation when a lower mass component transfers mass to its heavier companion (Marsh et al. 2004; Gokhale et al. 2007; Kremer et al. 2017). Because of the properties of degenerate matter, the lower mass star is the largest, and hence will be the first to fill its Roche lobe, and is thus the mass donor in the system. The mass transfer in turn depends on the details of how the donor responds to the mass

loss, which is sensitive to its structure and evolutionary state at the onset of mass transfer.

In the context of direct impact accretion models for HM Cnc a number of puzzles were initially noted. First, a fully degenerate donor will expand upon mass loss. The typical, long-term evolutionary behavior for such a system, assuming that mass transfer is stable, is for the orbital separation to grow with time ($\dot{f} < 0$), but this is opposite to the behavior observed in HM Cnc. Because in this case the timescale for growth in the mass transfer rate, $\dot{m}_2/\ddot{m}_2$ (here, m_2 is the donor mass), is much shorter than the overall mass transfer timescale, $m_2/\dot{m}_2 \propto J_{orb}/\dot{J}_{GR}$, the initial turn-on phase after contact during which the orbit continues to shrink ($\dot{f} > 0$) is very short, likely <100 yr (Priedhorsky & Verbunt 1988; Ritter 1988; Marsh et al. 2004; Willems & Kalogera 2005). Second, the long-term, quasi-stationary mass accretion rate $\dot{m}_2$ that is expected due to the loss of orbital angular momentum to gravitational radiation appears to be substantially larger than the rate estimated from the observed X-ray luminosity of ≈ 1–$2 \times 10^{33} d_{kpc}^2$ (here, d_{kpc} is the distance in kpc; Israel et al. 2003; Strohmayer 2008); though, we note that the distance to HM Cnc remains rather uncertain (Kupfer et al. 2018). These issues suggested a "fine-tuning" problem for a purely degenerate helium donor in that one might expect a low, a priori probability to observe a system in the very brief mass accretion turn-on phase, but see Willems & Kalogera (2005) for a discussion of how some of these problems could be alleviated.

Recent evolutionary calculations have further addressed these concerns. For example, Deloye et al. (2007) have used full stellar structure calculations coupled to the binary evolution to explore the evolution of helium white dwarf channel AM CVn binaries. They show that after the initiation of mass transfer the donors in these systems continue to shrink for a significant time (10^4–10^6 yr). During this $\dot{m}$ turn-on phase, $\dot{m}$ increases, and the binary eventually reaches a minimum period, after which the orbit expands as mass transfer eventually wins out over gravitational radiation. The details of the evolution, for example, the length of the initial turn-on phase, and the $\dot{m}$ evolution, depend on the entropy structure of the donor at contact.

Other proposed models have explored double white dwarf binary evolution in the case where the donor is a low mass He-core white dwarf but retains a substantial hydrogen-burning (p–p chain) envelope. Indeed, D'Antona et al. (2006) explored the evolution of such binaries and suggested that they could perhaps account for the observed properties of HM Cnc. These systems also show a much longer $\dot{m}$ turn-on phase since the donors contract upon mass loss until the hydrogen shell is removed. During this phase the orbit continues to shrink and $\dot{m}$ is also substantially less than that expected from a fully degenerate helium white dwarf. Evolutionary models for similar systems have also been computed by Kaplan et al. (2012).

Interestingly, optical spectroscopy of HM Cnc provides some evidence for the presence of hydrogen. While He emission lines are indeed present (Israel et al. 2002; Roelofs et al. 2010), Norton et al. (2004) pointed out that the line fluxes of the odd terms of the He II Pickering series were significantly reduced compared to neighboring even term transitions, and that this could result from blending of the even term lines with H Balmer lines. Subsequent modeling of high resolution spectra by Reinsch et al. (2007) appears to support this conclusion, and they derived an abundance ratio (by number)

of (He/H) ≈ 0.1. Additional spectroscopic observations and modeling would be valuable to confirm the presence of hydrogen in HM Cnc and better constrain the relative abundances of hydrogen and helium.

A key prediction in the evolution for these direct impact accretion models is that after the $\dot{m}$ turn-on phase, eventually, the orbital $\dot{f}$ should change sign. This can, in principle, be observationally tested by measuring or placing constraints on the second derivative of the orbital frequency, $\ddot{f}$. The sign and magnitude of $\ddot{f}$ will depend on the evolutionary stage of such a system. In the early turn-on stage the orbit evolution is not significantly affected by the mass accretion, and for a system with the orbital frequency of HM Cnc one would expect a positive $\ddot{f}_{gr} \approx 1 - 2 \times 10^{-28}$ Hz s^{-2} (Deloye & Taam 2006). However, if the mass turn-on is more developed, and mass transfer starts to influence the orbital evolution, then eventually $\ddot{f}$ should become negative and drive $\dot{f}$ toward zero. Depending on how close the system is to the maximum orbital frequency ($\dot{f} = 0$), the magnitude of $\ddot{f}$ could be substantially larger than $\ddot{f}_{gr}$ above, but with opposite sign (Deloye & Taam 2006; Deloye et al. 2007; Kaplan et al. 2012). Thus, a measurement of $\ddot{f}$ will provide clues to the evolutionary state of the mass turn-on phase, $\dot{f}/\ddot{f}$, and could allow estimates of the maximum orbital frequency and the rate at which $\dot{m}$ from the donor is evolving, that is, $\ddot{m}$, quantities which to our knowledge have never been inferred directly before.

Phase coherent timing of HM Cnc provides a unique opportunity for such measurements because the timing baseline is now approaching 20 years, and the phase drift associated with $\ddot{f}$ scales as $\Delta\phi = (1/6)\ddot{f}(t - t_0)^3$. For example, values of $\ddot{f} = 1 \times 10^{-27}$ Hz s^{-2} and $t - t_0 = 20$ yr give $\Delta\phi \approx 0.04$ cycles, which is larger than typical X-ray timing residuals (rms) of about 0.01 cycles for HM Cnc (Strohmayer 2005). Because of this we have been carrying out new timing observations of HM Cnc with the Neutron Star Interior Composition Explorer (NICER). Here we report on these new measurements that indicate that the orbital spin-up is slowing, with $\ddot{f} = -8.95 \pm 1.4 \times 10^{-27}$ Hz s^{-2}. The paper is organized as follows. In Section 2 we describe the new NICER data, including the results of a timing analysis that employs only these new data. In Section 3 we describe our new phase coherent timing solution that combines the prior Chandra data and the new NICER data. In Section 4 we discuss the implications of our findings for the evolutionary state and future evolution of HM Cnc. We conclude in Section 5 with a brief summary of our findings.

2. New NICER Observations

NICER was installed on the International Space Station in 2017 June, and began science observations after a one month checkout and verification period. NICER is designed for low background, high throughput, fast timing observations across the 0.2–12 keV band (Gendreau et al. 2012), achieving an absolute timing precision of ≈ 100 ns with the aid of a GPS receiver.

We obtained NICER observations of HM Cnc as part of a science team investigation to continue to monitor its orbital frequency. The first of these observations occurred in 2017 October. This program continued with additional observations in 2017 November, and 2018 April and December. These observations encompass observation IDs (obsids) 11020101nn, where nn ranges from 01 to 12. In addition to these observations, we also employ data obtained from NICER Guest Observer observations under Cycle 1 and 2 programs
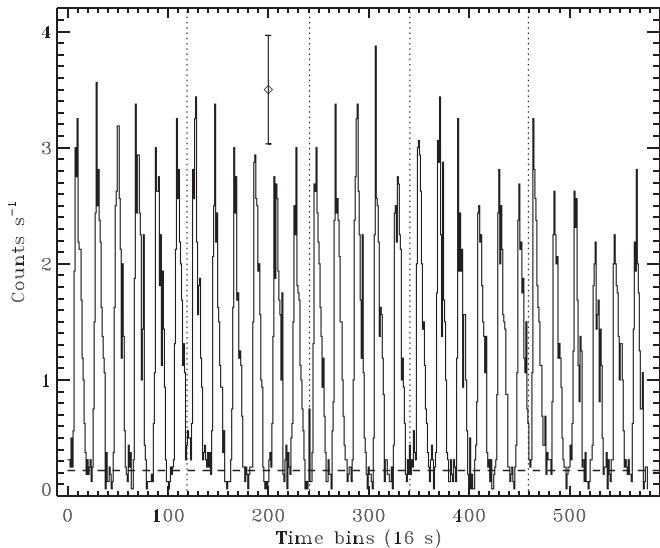
Figure 1. Light curve of HM Cnc from NICER observations obtained in 2020 April (obsid 3547010101). Data are the 0.3–1 keV band count rates measured in bins of 16 s length. In order to show a sample of pulses the time gaps have been removed. The start of each new GTI segment is indicated by a vertical dotted line. The horizontal dashed line is an estimate of the background level. We remind the reader that the x-axis does not have units of time, but rather time bin number.

(PI: Strohmayer) whose primary goal was the continuation of the long-term monitoring of the orbit. These observations occurred in 2019 May and November under obsids 2520010101 and 2520010201, and in 2020 April and November under obsids 3547010101, 3547010201, and 3547010202. We employed standard data filtering characteristics, using NICERDAS v7 (within HEASOFT 6.27), to screen the data, but with a few exceptions. We found that relaxing the standard criteria for so-called "undershoots" (a proxy for high optical loading) resulted in less fragmenting of some good time intervals (GTIs). We then visually inspected the 0.3–1 keV count rates (where the flux from HM Cnc resides), sampled at 1 s, for each GTI to confirm that no strong background variations were present. Finally, we ignored GTIs that were not longer than the 321.5 s pulse period of HM Cnc. This resulted in a final data selection of approximately 94 ks.

We barycentered the data using the *barycorr* tool employing the *JPLEPH.430* ephemeris and source coordinates (J2000) of R.A. = 121°5956 and decl. = 15°4586. The pulsing behavior of HM Cnc in the soft X-ray band is immediately apparent in the NICER light curves. As an example we show in Figure 1 the light curve in the 0.3–1 keV band for several consecutive dwells from obsid 3547010101. In this case we show the measured count rates in bins of 16 s length. In order to show a larger sample of pulses we removed the time gaps, and here the start of each new GTI segment is indicated by a vertical dotted line. We emphasize that the x-axis does *not* have units of time, but rather time bin number. We used the so-called 3C 50 background estimator, *nibackgen3C50*,[1] to estimate the background level for these data. That prediction is shown as the horizontal dashed line. The 321.5 s pulses are clearly evident, reaching a typical peak count rate of about 3 counts s^{-1}. One can also see that the off-pulse rate is approximately consistent with the estimated background, with occasional variations at

---

[1] https://heasarc.gsfc.nasa.gov/docs/nicer/tools/nicer_bkg_est_tools.html

Table 1
Timing Parameters for HM Cnc

Parameter	Value
Right ascension, α (J2000)	121°5956
Declination, δ (J2000)	15°4586
NICER epoch data only	...
Epoch, MJD (TDB)	58040.50761666807
Pulse frequency, f_0 (Hz)	0.0031102919 ± 0.14 nHz
Frequency derivative, $\dot{f}_0$ (Hz s^{-1})	$3.49 \pm 0.03 \times 10^{-16}$
Maximum Z_7^2	91107.3
Chandra and NICER data	3 parameter
Epoch, MJD (TDB)	53009.889943753
Pulse frequency, f_0 (Hz)	0.00311013797 ± 0.07 nHz
Frequency derivative, $\dot{f}_0$ (Hz s^{-1})	$3.557 \pm 0.005 \times 10^{-16}$
Frequency second derivative, $\ddot{f}_0$ (Hz s^{-2})	$-8.95 \pm 1.4 \times 10^{-27}$
Maximum Z_7^2	121056.3
Chandra and NICER data	2 parameter
Epoch, MJD (TDB)	53009.889943753
Pulse frequency, f_0 (Hz)	0.00311013820 ± 0.07 nHz
Frequency derivative, $\dot{f}_0$ (Hz s^{-1})	$3.533 \pm 0.004 \times 10^{-16}$
Maximum Z_7^2	120781.9

Note. Parameter uncertainties for f_0, $\dot{f}_0$, and $\ddot{f}_0$ are estimated as 1σ ($\Delta Z_7^2 = 7$) values.

the level of about 0.1–0.2 counts s^{-1}, indicative of some modest time-dependent variations in the NICER background.

3. Pulse Timing Analysis

We carry out a coherent timing study using the Z^2 statistic (Buccheri et al. 1983). We also refer the reader to our previous studies of HM Cnc and V407 Vul, and references therein, for details of the method (Strohmayer 2004, 2005). We begin by considering only the new NICER data. We use a two parameter phase timing model of the form $\phi(t) = f_0(t - t_0) + \frac{1}{2}\dot{f}_0(t - t_0)^2$. We carry out a grid search in the space of f_0 and $\dot{f}_0$, in order to find the parameter pair that maximizes the Z_7^2 statistic. We use the previously measured ephemeris to inform our search grid (Strohmayer 2005). The NICER data span a temporal baseline of about 1100 days, and the now well-known spin-up of the X-ray pulsation is clearly required to model the pulse phases. Results of our two parameter modeling are reported in Table 1, and Figure 2 shows contours of $\Delta Z_7^2 = \text{Max}(Z_7^2(f_0, \dot{f}_0)) - Z_7^2(f_0, \dot{f}_0)$ in the vicinity of our best solution, with contours drawn at values of 7, 14, and 21. This model provides an excellent description of the pulse timing, and the phase residuals with respect to this model are shown in Figure 3. Here, the top panel shows the phase residuals with respect to a model with constant frequency (that is, $\dot{f}_0 = 0$), and one can clearly see the remaining, downward-opening quadratic trend that is indicative of a positive $\dot{f}_0$. The lower panel shows the residuals with respect to the best two parameter model reported in Table 1.

Interestingly, the value of $\dot{f}_0$ inferred from the NICER data alone is less than the value determined from the Chandra epoch data. The difference between these two measurements is $3.49 \times 10^{-16} - 3.63 \times 10^{-16} = -0.14 \times 10^{-16}$ Hz s^{-1}. The magnitude of this difference is 2.3 times the reported uncertainty (0.06×10^{-16} Hz s^{-1}) of the Chandra measurement (Strohmayer 2005),
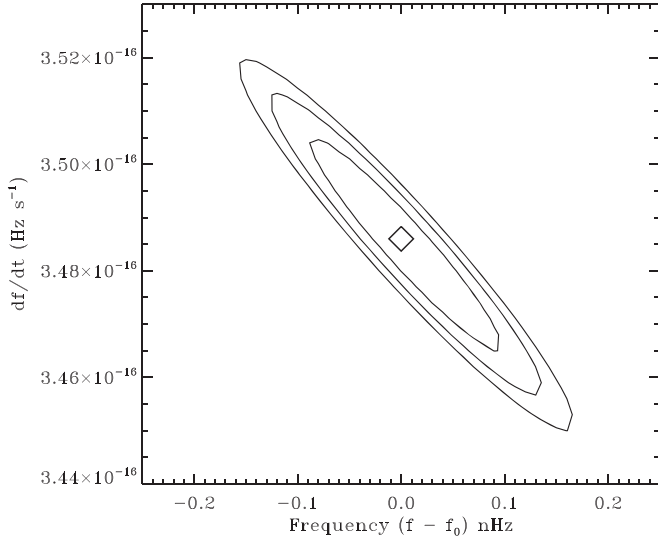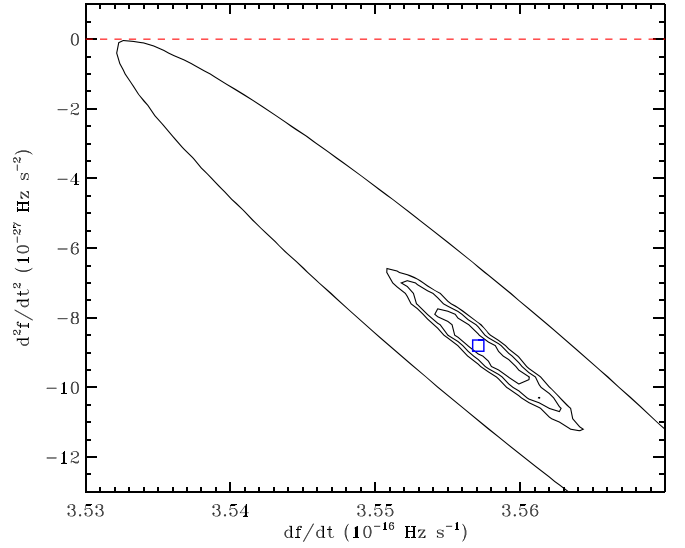
Figure 2. Contours of constant values of $\Delta Z_7^2 = \text{Max}(Z_7^2(f_0, \dot{f}_0)) - Z_7^2(f_0, \dot{f}_0)$ in the vicinity of our best two parameter solution for the phase timing model employing only the NICER epoch data, Here, $\dot{f}_0 = df/dt$. Contours are drawn at values of 7, 14, and 21.
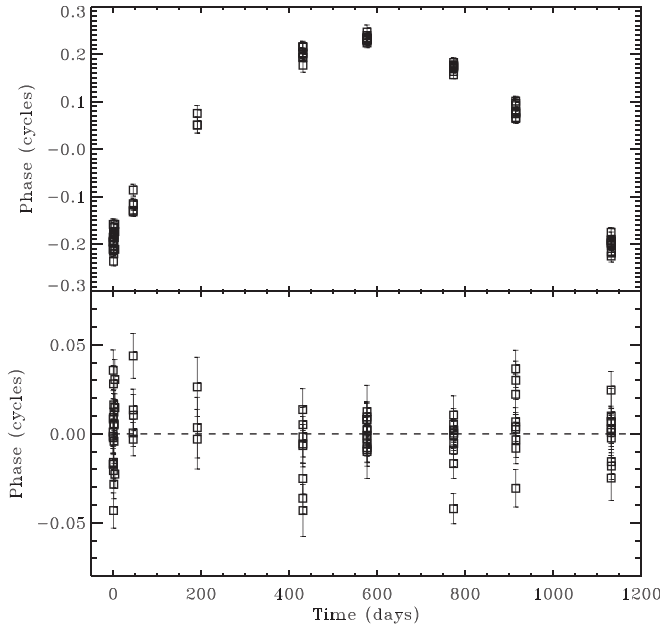
Figure 3. Phase timing residuals for HM Cnc obtained using the NICER epoch data only. The top panel shows the residuals with respect to a model with constant frequency (that is, with $\dot{f}_0 = 0$). Here, the downward-opening quadratic trend is indicative of a positive $\dot{f}_0$. The lower panel shows the residuals with respect to the best two parameter model reported in Table 1.

and 4.3 times the uncertainty of the NICER epoch measurement reported here. While not very significant on its own, it is suggestive of a secular decrease in the spin-up rate between the Chandra and NICER epochs, that could be produced by a negative $\ddot{f}$. The rough magnitude of the suggested change is then $\Delta \dot{f} / \Delta T = -0.14 \times 10^{-16} / (5030.6 \text{ days} \times 86400 \text{ s d}^{-1}) = -3.2 \times 10^{-26} \text{ Hz s}^{-2}$. Next we combine the Chandra and NICER data to carry out a coherent timing analysis using the full timing baseline, which is much more sensitive to a nonzero $\ddot{f}$ than either data set taken in isolation.

Figure 4. Contours of constant values of $\Delta Z_7^2 = \text{Max}(Z_7^2(f_0, \dot{f}_0, \ddot{f}_0)) - Z_7^2(f_0, \dot{f}_0, \ddot{f}_0)$ are shown in the $\ddot{f}_0 = d^2f/dt^2$ vs. $\dot{f}_0 = df/dt$ plane for our best three parameter timing model that uses both the Chandra and NICER epoch data. The inner contours are drawn at $\Delta Z_7^2 = 7$, 14, and 21, and the outer contour shows $\Delta Z_7^2 = 274.3$, which is the value obtained when $\ddot{f}_0 = 0$. See the text for additional details.

3.1. Phase Coherent Timing with Chandra and NICER

The basic method is the same as described above; however, we now employ a three parameter phase model of the form,

$$\phi(t) = f_0(t - t_0) + \frac{1}{2}\dot{f}_0(t - t_0)^2 + \frac{1}{6}\ddot{f}_0(t - t_0)^3. \quad (1)$$

The Chandra data is the same as described by Strohmayer (2005), to which we refer the reader for details. In addition, to facilitate comparisons we use the same reference epoch, t_0, as in Strohmayer (2005). We again carry out grid searches to find the parameter values that maximize Z_7^2. We use f_0 and $\dot{f}_0$ grids that comfortably encompass the range of values spanned by the prior solutions, and we search $\ddot{f}_0$ in the range from $\pm 4 \times 10^{-26}$ Hz s^{-2}, which conservatively covers the range expected based on theoretical considerations.

We began by fixing $\ddot{f}_0 = 0$ and searched for the f_0 and $\dot{f}_0$ pair, which yields the maximum Z_7^2. This best two parameter solution is summarized in Table 1, and is broadly consistent with the previous Chandra ephemeris, but with some indication of a smaller $\dot{f}_0$, as also suggested by our timing of the NICER data alone. Next, we searched the full three parameter space to try and determine whether a better solution exists—in the context of yielding a larger maximum value of Z_7^2—with a nonzero value for $\ddot{f}_0$. This analysis indeed resulted in an improved fit, with an increase in Z_7^2 of 274.3, for $\ddot{f}_0 = -8.95 \times 10^{-27}$ Hz s^{-2}. This best three parameter ephemeris is also summarized in Table 1. We emphasize that the statistical (Poisson) noise distribution for Z_7^2 is a χ^2 distribution with 14 degrees of freedom, and an increase of 274.3 is extremely unlikely to be produced simply by chance. This provides compelling evidence for a negative $\ddot{f}_0$ in the system. Figure 4 shows a contour plot of $\Delta Z_7^2 = \text{Max}(Z_7^2(f_0, \dot{f}_0, \ddot{f}_0)) - Z_7^2(f_0, \dot{f}_0, \ddot{f}_0)$ in the $\ddot{f}_0$ versus $\dot{f}_0$ plane, where for each $\ddot{f}_0$ and $\dot{f}_0$ pair we have selected the maximum value of Z_7^2 by searching over the remaining parameter, f_0. The inner contours are drawn at $\Delta Z_7^2 = 7$, 14, and 21, and the outer contour shows
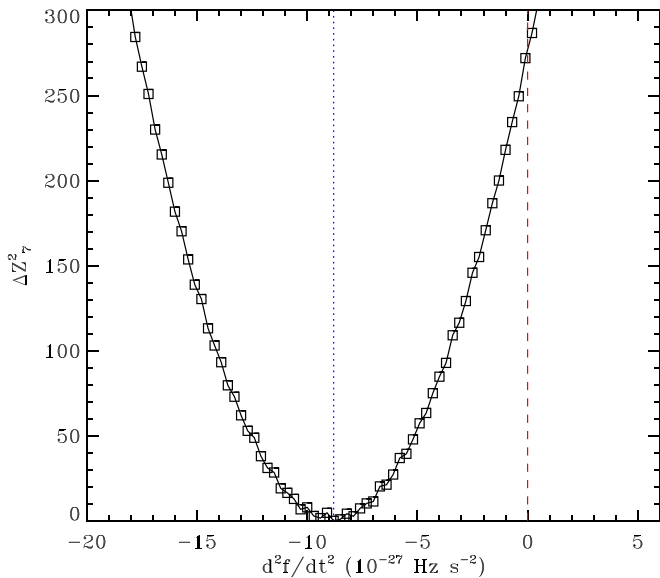
Figure 5. The run of $\Delta Z_7^2 = \mathrm{Max}(Z_7^2(f_0, \dot{f}_0, \ddot{f}_0)) - Z_7^2(f_0, \dot{f}_0, \ddot{f}_0)$ as a function of $\ddot{f}_0 = d^2f/dt^2$ for our best three parameter timing model that uses both the Chandra and NICER epoch data. For each value of $\ddot{f}_0$ the two other parameters are marginalized over by selecting the maximum value of Z_7^2. The vertical dotted line (blue) marks the best solution for $\ddot{f}_0$, and the value $\ddot{f}_0 = 0$ is marked by the vertical dashed (red) line.

$\Delta Z_7^2 = 274.3$, which is the value obtained when $\ddot{f}_0 = 0$. Figure 5 shows the run of ΔZ_7^2 as a function of only $\ddot{f}_0$, where we have marginalized over the two other parameters by again selecting the maximum value of Z_7^2. This plot also shows how a negative, nonzero value of $\ddot{f}$ clearly results in a better fit to the timing data.

Figure 6 shows the phase timing residuals employing our best three parameter solution (black symbols). The model provides an excellent description of the phase timing data, with an rms residual of 0.0144 cycles. In addition, we also computed residuals using the best two parameter solution (that is, with $\ddot{f}_0 = 0$). The red symbols plotted beneath the three parameter solution represent the difference between the residuals of the full three parameter fit and those from the two parameter result. These have been displaced by -0.075 cycles for clarity. This difference shows the clear systematic cubic trend in the phase residuals that remains when one uses a model with only f_0 and $\dot{f}_0$, and further emphasizes the need for a significant cubic term (that is, a nonzero $\ddot{f}_0$) in the phase model.

Using our best three parameter timing model we computed phase-folded profiles for both the Chandra and NICER epoch data. Figure 7 shows two examples of each profile. The top panel shows the observed total counts as a function of phase. In the lower panel we have first fit the off-pulse, mean levels and then subtracted them. The Chandra profile is then multiplied by a factor of 3.45 and overplotted in order to make a closer comparison between the two profiles. This gives a visual depiction of how well the two profiles are aligned, as well as indicating a high degree of stability to the pulse shape over almost two decades. Finally, to facilitate comparisons between the X-ray phase and orbital phase constraints that may be obtained from future gravitational wave measurements, we emphasize that the phase of the X-ray pulse can be predicted using Equation (1) and the parameter values in Table 1. We note that this is the X-ray phase as indicated in Figure 7.
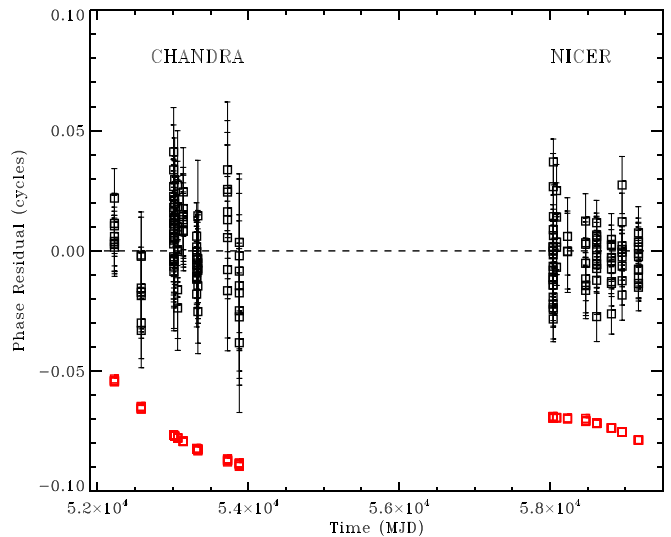
Figure 6. Phase timing residuals for HM Cnc obtained using our best three parameter model employing both the Chandra and NICER epoch data. The black square symbols with error bars show the residuals from the best three parameter solution $(f_0, \dot{f}_0, \ddot{f}_0)$ given in Table 1. The model provides an excellent description of the phase timing data, with an rms residual of 0.0144 cycles. The red symbols show the difference between the residuals of the full three parameter solution and those from the best two parameter results. These have been displaced by -0.075 cycles for clarity. This difference shows the clear, systematic cubic trend in the phase residuals that remains when one uses a model with only f_0 and $\dot{f}_0$, and further emphasizes the need for a significant cubic term (that is, a nonzero $\ddot{f}_0$) in the phase model.
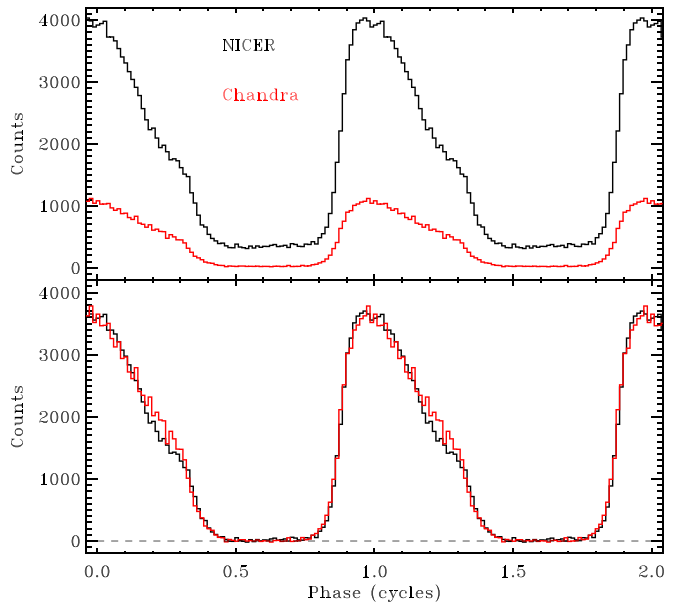
Figure 7. Phase-folded pulse profiles for both the Chandra and NICER epoch data using our best three parameter timing model (see Table 1). The top panel shows the observed total counts as a function of phase for both data sets. The bottom panel presents a closer comparison of the pulse profiles. First, the mean of the off-pulse emission is subtracted from each profile. The Chandra profile was then multiplied by a factor of 3.45 and overplotted. This gives a visual depiction of how well the two profiles are aligned, as well as indicating a high degree of stability to the pulse shape over almost two decades.

4. Implications and Discussion

The analysis above demonstrates that the orbital frequency of HM Cnc is still increasing, but that the rate of increase is slowing, and it provides an estimate of the future orbital

frequency evolution of the system. Our timing model predicts,

$$f(t) = f_0 + \dot{f}_0(t - t_0) + \frac{\ddot{f}_0}{2}(t - t_0)^2 \qquad (2)$$

and

$$\dot{f}(t) = \dot{f}_0 + \ddot{f}_0(t - t_0), \qquad (3)$$

where t_0 is the reference epoch (see Table 1). The measurement of a negative $\ddot{f}_0$ indicates that the orbital frequency will reach a maximum, f_{max}, when $\dot{f}(t)$ reaches zero. This will occur in a time $t_{f_{max}} - t_0 = -(\dot{f}_0/\ddot{f}_0) = 1259.7 \pm 200$ yr, when the maximum orbital frequency will be, $f_{max} = f_0 - (1/2)(\dot{f}_0^2/\ddot{f}_0) = 3.1172091$ mHz. This reveals the evolutionary phase of the binary, it is close to its maximum orbital frequency. Indeed, the current frequency is now 99.77% of the estimated maximum.

4.1. Comparison with Theoretical Models

Our results are plausibly consistent with evolutionary sequences of compact white dwarf binaries computed by several authors. In the context of the evolutionary calculations of AM CVn progenitor systems by Deloye et al. (2007), HM Cnc would be near the end of the so-called $\dot{m}$ turn-on phase, and near frequency maximum (period minimum). For example, plausible evolutionary tracks relevant for HM Cnc are shown in their Figures 16 and 18. Indeed, in Figure 18 (bottom), which shows the logarithm of $|\dot{P}_{orb}|$ as a function of the orbital period, P_{orb}, the yellow and cyan curves represent two possible scenarios, one (yellow curve) that is further from frequency maximum, and with a positive $\ddot{f}$, and the other (cyan curve) that is closer to frequency maximum, and with a negative $\ddot{f}$, similar to our finding above for HM Cnc. Here, the cyan model is clearly a better representation of a plausible evolutionary state of HM Cnc. This highlights the importance of $\ddot{f}$ measurements, as one now has an additional observable to constrain such evolutionary models, that is, a consistent model should pass through the measured f and $\dot{f}$ values while also having the right slope ($\ddot{f}$) at that point.

Additional models have been computed by D'Antona et al. (2006) and Kaplan et al. (2012) for low mass white dwarf donors that retain relatively thick hydrogen envelopes. This is an interesting difference from the models computed by Deloye et al. (2007), which comprise essentially hydrogen-free donors. These models with hydrogen envelopes show a similar overall orbital evolution compared to the Deloye et al. (2007) evolutions; however, their phases of orbital frequency increase tend to be longer and at a bit lower $\dot{m}$. Example evolutions can be seen in Figures 2 and 6 in D'Antona et al. (2006) and Kaplan et al. (2012), respectively.

4.2. X-Ray Spectrum, Flux, and Luminosity

An additional, important discriminator among these models is the mass accretion rate, $\dot{m}$. In principle, this can be estimated from the bolometric luminosity, which includes the observed X-ray luminosity. Prior X-ray spectral measurements of HM Cnc find that an ≈ 60 eV blackbody describes the spectrum well, and yields peak flux measurements in the range of 1.3–1.5×10^{-11} erg cm^{-2} s^{-1} (Israel et al. 2004; Strohmayer 2008). We extracted a NICER spectrum from the same GTIs (obsid 3547010101) that are shown in Figure 1, and we used the 3C 50 background estimator, *nibackgen3C50*, to estimate the background level for these data.
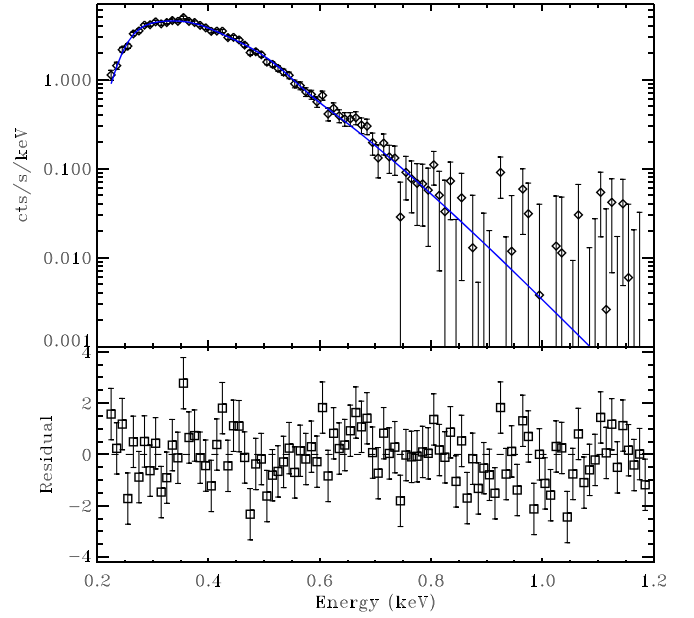
Figure 8. Time-averaged NICER spectrum obtained from obsid 3547010101. The top panel shows the count rate spectrum and best-fitting blackbody model (*tbabs∗bbodyrad* in XSPEC). The bottom panel shows the residuals, (Data—Model)/σ. See the text for additional details.

We used the most recent, publicly available response files to fit the 0.2–1.2 keV data using XSPEC version 12.11.1c_d. We find that an absorbed blackbody model (*tbabs∗bbodyrad* in XSPEC) provides an excellent fit to the spectrum ($\chi^2 = 98.5$ with 94 degrees of freedom), with $kT_{bb} = 59 \pm 1$ eV and an estimated flux (0.1–2.5 keV) per NICER count rate of 4.7×10^{-12} erg cm^{-2} s^{-1}. We also find $n_H = 0.032 \pm 0.002 \times 10^{22}$ cm^{-2}. Figure 8 shows a plot of the NICER spectrum, with the observed count rate spectrum and best-fitting model shown in the top panel, and the residuals to the best-fitting model in the bottom panel. To estimate the peak X-ray flux, we simply multiply the flux measurement above by the peak NICER count rate, which is typically in the range from 3–3.4 s^{-1}. This gives a flux estimate in the range from 1.4–1.6×10^{-11} erg cm^{-2} s^{-1}, that is approximately within the range of prior measurements. This implies an X-ray luminosity of 1.68–$1.91 \times 10^{33}(\Delta\Omega/4\pi)d_{kpc}^2$ erg s^{-1}, where d_{kpc} is the distance in kiloparsecs and $\Delta\Omega$ is the solid angle into which the flux is radiated.

The blackbody fit above yields a normalization, $K = R_{km}^2/d_{10}^2 = 41148 \pm 4700$, where R_{km} is the radius of a sphere that radiates the blackbody flux, and d_{10} is the distance in units of 10 kpc. If we estimate the surface emitting area on the accretor as $S_{em} = 4\pi R_{km}^2$, we can then estimate the fraction of the surface area of the accretor that is radiating the soft X-ray flux as, $f_{area} = K d_{10}^2(C_p/C_{avg})/R_1^2$, where R_1 is the accretor radius, and C_p/C_{avg} represents the ratio of peak to average count rates, since we derived the flux (and normalization) above by fitting to the time-averaged spectrum. This gives a value of $f_{area} = 0.001 d_{10}^2$, where we have used $C_p = 3$ and $R_1 = 0.015 R_\odot$. While the precise value is sensitive to the distance, the prefactor is roughly consistent with the small spot size anticipated for direct impact accretion (Marsh & Steeghs 2002).

To convert a flux to a luminosity requires knowledge of the distance. Unfortunately, there is significant uncertainty regarding the distance to HM Cnc. Early X-ray luminosity estimates

assumed the source was relatively nearby, with $d < 1$ kpc. The source is too faint for a parallax measurement with Gaia, and Kupfer et al. (2018) suggested a distance of order 5 kpc or greater based largely on theoretical considerations (Bildsten et al. 2006; D'Antona et al. 2006). Interestingly, Barros et al. (2007) used optical spectroscopy to constrain the temperature of the heated face of the donor, and, under the assumption that either X-ray or optical/UV irradiation from the accretor is responsible for heating the donor, derived a lower limit to the bolometric luminosity. Based on this they suggested limits on the distance of $d > 1.1$ and $d > 4.2$ kpc, respectively.

We estimate the mass accretion rate under the assumption that the accretion luminosity results from the difference in gravitational potential energy of matter at the inner Lagrangian point and the surface of the accretor. For this we use the prescription of Han & Webbink (1999). Taking $1.8 \times 10^{33}(\Delta\Omega/4\pi)d_{kpc}^2$ erg s^{-1} as a typical luminosity for HM Cnc, this converts to a mass accretion rate of $\dot{m} = 6.2 \times 10^{-10}(\Delta\Omega/4\pi)d_{kpc}^2 M_\odot$ yr^{-1}, where we have used representative masses of 0.56 and $0.26 M_\odot$ for the accretor and donor, respectively (Roelofs et al. 2010). For a distance of 5 kpc we would infer $\dot{m} \approx 1.6 \times 10^{-8} M_\odot$ yr^{-1}, which is roughly consistent with the accretion rates predicted by the binary evolution models discussed above as they approach orbital frequency maximum.

4.3. Implications for M_1, M_2, and $\ddot{M}_2$

The precise measurement of f and $\dot{f}$, as well as constraints on $\dot{m}$ allow us to place constraints on the component masses. Under the assumption of conservative mass transfer the orbital frequency varies as,

$$\dot{f} = -3f\left[\frac{\dot{J}}{J} - (1 - q)\frac{\dot{M}_2}{M_2}\right], \tag{4}$$

where M_1 and M_2 are the accretor and donor masses, respectively, $q = M_2/M_1$ is the mass ratio, $\dot{M}_2$ is the donor's mass loss rate, and,

$$\frac{\dot{J}}{J} = -\frac{32}{5}\frac{G^3}{c^5}\frac{M_1 M_2(M_1 + M_2)}{a^4}, \tag{5}$$

is the angular momentum loss rate due to gravitational radiation from a circular orbit (Landau & Lifshitz 1971).

Note that both $\dot{M}_2 = -\dot{m}$ and $\dot{J}/J$ are < 0. This shows that the gravitational radiation term, $\dot{J}/J$, acts to increase the orbital frequency ($\dot{f} > 0$), while the $\dot{M}_2$ term acts to decrease the frequency ($\dot{f} < 0$). We also note that the equation above assumes that the angular momentum associated with the accretion stream is transferred back to the orbit. This is generally thought to be efficiently achieved via tidal forces acting on an accretion disk (Priedhorsky & Verbunt 1988). In the case of direct impact accretion, it is not currently known how efficiently this transfer occurs. If there is no transfer of this angular momentum back to the orbit, then an additional term should appear in Equation (4) that acts to reduce the dominant $(1 - q)(\dot{M}_2/M_2)$ term by an amount, $((1 + q)r_h)^{1/2}(\dot{M}_2/M_2)$, where $r_h = R_h/a$ represents the radius around the accretor with the same specific angular momentum as the accreted material. We have used the prescription of Verbunt & Rappaport (1988) to compute r_h and find that for parameters relevant to the current evolutionary state of HM Cnc, this indeed represents a modest reduction in the dominant mass transfer term. In the remainder of the discussion we will neglect this term. For a
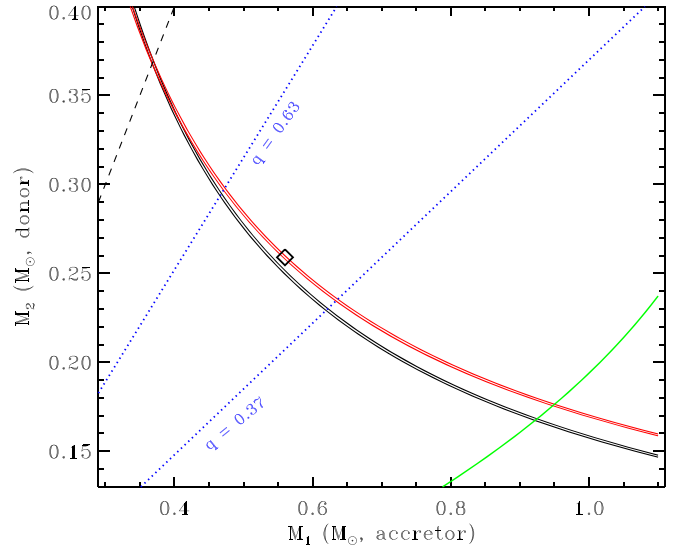
Figure 9. Constraints on the component masses of HM Cnc based on the measured $\dot{f}_0$ from our full three parameter timing model (see Table 1). Here, the contours enclose regions of parameter space that are consistent with $\dot{f}_0 = 3.557 \pm 0.005 \times 10^{-16}$ Hz s^{-1}. The black curves are derived assuming $\dot{M}_2 = 0$, while the red curves were computed assuming $\dot{M}_2 = -1.6 \times 10^{-8} M_\odot$ yr^{-1}, which is the inferred accretion rate assuming a distance of 5 kpc to HM Cnc. The region enclosed by the blue dotted lines is consistent with the mass ratio limits derived by Roelofs et al. (2010). The green curve denotes the boundary between direct impact and disk accretion from Sepinsky & Kalogera (2014). The diamond symbol marks the M_1 and M_2 values used for the mass accretion rate estimates discussed in the text.

more complete discussion of the angular momentum transfer in close white dwarf binaries we refer the reader to Marsh et al. (2004) and Kremer et al. (2017).

Figure 9 illustrates the constraints on the component masses based on the measured $\dot{f}_0$ from our full three parameter timing model (see Table 1). Here, the contours enclose regions of parameter space that are consistent with $\dot{f}_0 = 3.557 \pm 0.005 \times 10^{-16}$ Hz s^{-1}. The black curves are derived assuming $\dot{M}_2 = 0$, while the red curves were computed with $\dot{M}_2 = -1.6 \times 10^{-8} M_\odot$ yr^{-1}, which is the inferred rate above assuming a distance of 5 kpc to HM Cnc. The blue dotted lines mark lines of constant mass ratio, q, and denote the mass ratio limits derived by Roelofs et al. (2010) from their optical spectroscopy and radial velocity measurements. The black diamond symbol marks the representative values of $M_1 = 0.56$ and $M_2 = 0.26 M_\odot$ used for our accretion rate estimate above. The green curve denotes the boundary between direct impact and disk accretion from Sepinsky & Kalogera (2014). This shows that even for mass accretion rates consistent with a 5 kpc distance, the frequency evolution is still mostly set by the loss of angular momentum to gravitational radiation. We show in Figure 10 a plausible schematic of the system, where we have plotted the Roche lobe contours for component masses of 0.56 and $0.26 M_\odot$ for the accretor and donor, respectively. Here, the donor is located at $x = 0$, and the center of mass is marked with an "x" symbol. The size of the accretor is denoted by the red circle, and is estimated using the white dwarf mass versus radius relation as approximated by Nelemans et al. (2001). The cyan circle is an estimate of the limiting radius for direct impact accretion to occur, and is obtained from the relation of Sepinsky & Kalogera (2014). The dashed curve is an estimate of the trajectory of the accretion stream. It is not the result of a dynamical calculation, but is meant as a pedagogical guide only. Finally, we note that at
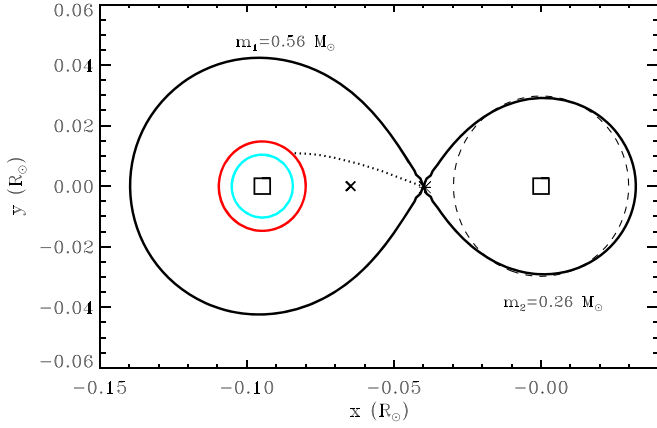
Figure 10. Roche lobe contours for a system like HM Cnc with component masses of 0.56 and 0.26 $M_\odot$ for the accretor and donor, respectively. Here, the donor is located at $x = 0$, and the center of mass is marked with an "x" symbol. The size of the accretor is denoted by the red circle, and is estimated using the white dwarf mass vs. radius relation as approximated by Nelemans et al. (2001). The cyan circle is an estimate of the limiting radius for direct impact accretion to occur, and is obtained from the relation of Sepinsky & Kalogera (2014). The dashed curve is an estimate of the trajectory of the accretion stream. It is not the result of a dynamical calculation, but is meant as a pedagogical guide only.

the present rate of orbital frequency increase the orbital separation is shrinking at a rate $\dot{a} = -(2/3)(\dot{f}_0/f_0)a \approx 0.16$ km yr^{-1}.

Adopting the same conservative mass transfer prescription as above, we can determine $\dddot{f}$ via differentiation of Equation (4) as,

$$\dddot{f} = -3\dot{f}\left(\frac{\dot{J}}{J} - (1 - q)\frac{\dot{M}_2}{M_2}\right)$$

$$+ \frac{96G^3 M_1 M_2 (M_1 + M_2)f}{5c^5 a^4}\left((1 - q)\frac{\dot{M}_2}{M_2} + \frac{8\dot{f}}{3f}\right) \quad (6)$$

$$+ \frac{3f(1 - q)}{M_2^2}(M_2\ddot{M}_2 - \dot{M}_2^2) - \frac{3f(1 + q)\dot{M}_2^2}{M_1 M_2}, \quad (7)$$

where the symbols have the same meanings defined above, and $\ddot{M}_2$ is the rate of change of the mass accretion rate from the donor. From this expression we can see that a measurement of $\dddot{f}$ implies a constraint on $\ddot{M}_2$. If we assume $\dot{M}_2 = -1.6 \times 10^{-8} M_\odot$ yr^{-1}, which is the rate derived above based on assuming a distance of 5 kpc, then from this expression we would require $-5.4 \times 10^{-10} < \ddot{M}_2 < -4.0 \times 10^{-10}$ $M_\odot$ yr^{-2}, based on the $\pm 1\sigma$ bounds on $\dddot{f}_0$ derived above, and we have again used representative component masses of 0.56 and 0.26 $M_\odot$ for the accretor and donor, respectively. We note, however, that the inferred constraint on $\ddot{M}_2$ is not very sensitive to the assumed mass accretion rate.

Interestingly, if the conservative mass transfer modeling is appropriate, then this would suggest another indirect way to constrain the distance. The inferred $\dot{M}_2$ suggests a timescale to double the accretion rate of $t_{\rm double} = \dot{M}_2/\ddot{M}_2 \approx 39.2$ yr. This would suggest that one might expect to see an overall increase in X-ray brightness from HM Cnc over the current existing span of X-ray observations, assuming a simple linear relation between the mass accretion rate and the resulting X-ray flux. For example, the first detections of the source were obtained with the ROSAT HRI in late 1994 and early 1995

(Israel et al. 1999), about 25 yr ago. These authors quote a time-averaged flux in the range from $3–4.8 \times 10^{-12}$ erg cm^{-2} s^{-1} (0.5–2.0 keV); though, we note that this was based on assuming a Crab-like spectrum for the source. This can be compared with our time-averaged flux value of 4.7×10^{-12} erg cm^{-2} s^{-1} reported above. While it is difficult to draw precise conclusions based on this comparison, due to issues such as absolute flux calibration uncertainties, it tends to suggest that there has perhaps not been a marked increase in source brightness (and thus mass accretion rate) over these 25 yr.

If the magnitude of $\dot{M}_2$ were lower by a factor of 25, as would be anticipated if the source distance were only 1 kpc, then the inferred value of $\ddot{M}_2$ would increase only slightly, but, because of the smaller $\dot{m}$ this would then suggest that the timescale for the mass accretion rate to double would be only 1.6 yr. In such a case one would anticipate that long-term X-ray observations would have shown some secular increase in brightness, but as indicated above this does not seem to be the case. At face value this suggests the need for a mass accretion rate that is large enough so that one would not expect a significant increase in observed source X-ray luminosity (due to $\dot{M}_2$ growing in magnitude) over the observational history of the source. This then naturally also favors larger source distances. Clearly a better distance constraint for HM Cnc would be very informative, as would a more careful search for any long-term variability in the source. While further observations with Gaia may prove indecisive regarding the distance to HM Cnc, future observations of the gravitational radiation from the source with LISA should be able to provide an accurate distance. The key point here is that the precise measurement of $\dot{f}$ provides an accurate determination of the so-called chirp mass. The gravitational wave strain amplitudes in the two different polarizations are then a function only of the source distance and orbit plane inclination on the sky (Korol et al. 2017). Since the expected gravitational wave signal-to-noise ratio for HM Cnc with LISA is expected to be >100, even for distances as large as 10 kpc, it should be possible to measure the distance (Shah et al. 2012).

5. Summary

We have presented a study of new NICER observations of HM Cnc that extend the timing baseline of this source to almost 20 yr. When combined with existing Chandra data we find that a phase coherent timing analysis strongly requires a nonzero cubic term in the timing model, and we measure $\dddot{f}_0 = -8.95 \pm 1.4 \times 10^{-27}$ Hz s^{-2}, for the first time in any ultracompact accreting binary. This provides strong evidence that HM Cnc is an evolving compact white dwarf binary that is very close to its epoch of maximum orbital frequency (D'Antona et al. 2006; Deloye et al. 2007; Kaplan et al. 2012), and we estimate that the source will reach this epoch in $\approx 1260 \pm 200$ yr. Assuming that mass transfer is conservative, and that the observed $\dddot{f}$ is largely set by the time rate of change of the mass accretion rate from the donor, $\ddot{M}_2$, we place a constraint on this quantity of, $-5.4 \times 10^{-10} < \ddot{M}_2 < -4.0 \times 10^{-10}$ $M_\odot$ yr^{-2}, that is not very sensitive to the assumed accretion rate. A better constraint on the source distance should enable tighter constraints on the mass accretion rate and hence models for the evolution of this and similar sources. Continued timing with NICER will enable greater precision on the $\dddot{f}_0$ measurement, and long-term flux measurements would also be valuable.

Facilities: NICER, ADS, HEASARC.

Software: HEAsoft (v6.27; Arnaud 1996).

ORCID iDs

Tod E. Strohmayer ⓘ https://orcid.org/0000-0001-7681-5845

References

Amaro-Seoane, P., Audley, H., Babak, S., et al. 2017, arXiv:1702.00786
Arnaud, K. A. 1996, in ASP Conf. Ser. 101, Astronomical Data Analysis Software and Systems V, ed. G. H. Jacoby & J. Barnes (San Francisco, CA: ASP), 17
Barros, S. C. C., Marsh, T. R., Dhillon, V. S., et al. 2007, MNRAS, 374, 1334
Bildsten, L., Townsley, D. M., Deloye, C. J., & Nelemans, G. 2006, ApJ, 640, 466
Buccheri, R., Bennett, K., Bignami, G. F., et al. 1983, A&A, 128, 245
D'Antona, F., Ventura, P., Burderi, L., & Teodorescu, A. 2006, ApJ, 653, 1429
Deloye, C. J., & Taam, R. E. 2006, ApJL, 649, L99
Deloye, C. J., Taam, R. E., Winisdoerffer, C., & Chabrier, G. 2007, MNRAS, 381, 525
Gendreau, K. C., Arzoumanian, Z., & Okajima, T. 2012, Proc. SPIE, 8443, 844313
Gokhale, V., Peng, X. M., & Frank, J. 2007, ApJ, 655, 1010
Han, Z., & Webbink, R. F. 1999, A&A, 349, L17
Hils, D., & Bender, P. L. 2000, ApJ, 537, 334
Israel, G. L., Covino, S., Dall'Osso, S., et al. 2004, MSAIS, 5, 148
Israel, G. L., Covino, S., Stella, L., et al. 2003, ApJ, 598, 492
Israel, G. L., Hummel, W., Covino, S., et al. 2002, A&A, 386, L13
Israel, G. L., Panzera, M. R., Campana, S., et al. 1999, A&A, 349, L1
Kaplan, D. L., Bildsten, L., & Steinfadt, J. D. R. 2012, ApJ, 758, 64
Korol, V., Rossi, E. M., Groot, P. J., et al. 2017, MNRAS, 470, 1894
Kremer, K., Breivik, K., Larson, S. L., & Kalogera, V. 2017, ApJ, 846, 95
Kupfer, T., Korol, V., Shah, S., et al. 2018, MNRAS, 480, 302
Landau, L. D., & Lifshitz, E. M. 1971, The Classical Theory of Fields (Oxford: Pergamon Press)
Lubow, S. H., & Shu, F. H. 1975, ApJ, 198, 383
Marsh, T. R., Nelemans, G., & Steeghs, D. 2004, MNRAS, 350, 113
Marsh, T. R., & Steeghs, D. 2002, MNRAS, 331, L7
Nelemans, G., Portegies Zwart, S. F., Verbunt, F., & Yungelson, L. R. 2001, A&A, 368, 939
Nelemans, G., Yungelson, L. R., & Portegies Zwart, S. F. 2004, MNRAS, 349, 181
Norton, A. J., Haswell, C. A., & Wynn, G. A. 2004, A&A, 419, 1025
Priedhorsky, W. C., & Verbunt, F. 1988, ApJ, 333, 895
Reinsch, K., Steiper, J., & Dreizler, S. 2007, in ASP Conf. Ser. 372, Spectral Analysis and Constraints on the Nature of the Ultra-Compact Binary RX J0806.3+1527, ed. R. Napiwotzki & M. R. Burleigh (San Francisco, CA: ASP), 419
Ritter, H. 1988, A&A, 202, 93
Roelofs, G. H. A., Rau, A., Marsh, T. R., et al. 2010, ApJL, 711, L138
Sepinsky, J. F., & Kalogera, V. 2014, ApJ, 785, 157
Shah, S., van der Sluys, M., & Nelemans, G. 2012, A&A, 544, A153
Strohmayer, T. E. 2004, ApJ, 610, 416
Strohmayer, T. E. 2005, ApJ, 627, 920
Strohmayer, T. E. 2008, ApJL, 679, L109
Tutukov, A., & Yungelson, L. 1996, MNRAS, 280, 1035
Verbunt, F., & Rappaport, S. 1988, ApJ, 332, 193
Willems, B., & Kalogera, V. 2005, arXiv:astro-ph/0508218